12-2021

Respiratory Compensated Robot for Liver Cancer Treatment: Design, Fabrication, and Benchtop Characterization

Mishek Jair Musa
University of Arkansas, Fayetteville

Respiratory Compensated Robot for Liver Cancer Treatment: Design, Fabrication, and Benchtop Characterization

A thesis submitted in partial fulfillment
of the requirements for the degree of
Master of Science in Mechanical Engineering

by

Mishek Musa
University of Arkansas
Bachelor of Science in Mechanical Engineering, 2019

December 2021
University of Arkansas

This thesis is approved for recommendation to the Graduate Council.

Yue Chen, Ph.D.
Thesis Director

Uche Wejinya, Ph.D.
Committee Member

Han Hu, Ph.D.
Committee Member

Abstract

Hepatocellular carcinoma (HCC) is one of the leading causes of cancer-related death in the world. Radiofrequency ablation (RFA) is an effective method for treating tumors less than 5 cm. However, manually placing the RFA needle at the site of the tumor is challenging due to the complicated respiratory induced motion of the liver. This paper presents the design, fabrication, and benchtop characterization of a patient mounted, respiratory compensated robotic needle insertion platform to perform percutaneous needle interventions. The robotic platform consists of a 4-DoF dual-stage cartesian platform used to control the pose of a 1-DoF needle insertion module. The active needle insertion module consists of a 3D printed flexible fluidic actuator capable of providing a step-like, grasp-insert-release actuation that mimics the manual insertion procedure. Force characterization of the needle insertion module indicates that the device is capable of producing 22.6 ± 0.40 N before the needle slips between the grippers. Static phantom targeting experiments indicate a positional error of 1.14 ± 0.30 mm and orientational error of 0.99° ± 0.36°. Static ex-vivo porcine liver targeting experiments indicate a positional error of 1.22 ± 0.31 mm and orientational error of 1.16° ± 0.44°. Dynamic targeting experiments with the proposed active motion compensation in dynamic phantom and ex-vivo porcine liver show 66.3% and 69.6% positional accuracy improvement, respectively. Future work will continue to develop this platform with the long-term goal of applying the system to RFA for HCC.

Acknowledgements

Firstly, I would like to thank my graduate supervisor, Dr. Yue Chen, for his invaluable advice, continuous support, and patience during my graduate study. His dedication and plentiful experience have encouraged me in all aspects of my academic research and daily life. I would also like to thank Dr. Uche Wejinya and Dr. Han Hu for serving as members of my thesis committee and for their mentorship.

In addition to my advisory committee, I would like to thank all the members, past and present, of the Medical Robotics Lab for their kind help and support that have made my graduate study and life here at the UofA a wonderful time. It has been a pleasure getting to know and working with each and every one of you.

To all my friends here in the US and back home in Belize, thank you for always being a major source of support and motivation. The necessary distractions you provided from my research have made the past few years memorable. I am grateful to you for always being there for me.

Finally, I would like to express my deepest gratitude to my family for their continuous and unparalleled love and support. To my sister Mya, thank you for always being there for me. To my parents, Pamela and Yasser, without your tremendous understanding and encouragement, it would be impossible for me to complete my studies.

Table of Contents

1. Introduction

Primary liver cancer, also known as hepatocellular carcinoma (HCC), is the third most common cause of cancer-related death in the world with over 700,000 deaths reported annually [1]. In the United States, an estimated 42,000 adults are diagnosed with liver cancer each year, and the number of cases is expected to continue to rise due to the increasing number of chronic liver diseases caused by alcohol, nonalcoholic fatty liver disease, hepatitis B, and hepatitis C infection. The five-year survival rate for patients is as low as 4% [2]. As a result, there is a considerable economic loss of upwards of $1 billion per year in the United States [3].

HCC can be treated with a variety of methods. Medical therapy sorafenib provides no reduction to the mortality rate as it only prolongs survival for a few months [4]. Chemotherapy fails to provide effective treatment to control tumor growth, primarily due to HCC's resistance to radiation [5]. Liver transplantation and partial surgical resection have both been shown to be effective methods of treatment, however, they both require strict criteria for candidate selection, thus preventing the majority of diagnosed patients from receiving treatment [6, 7]. Stereotactic radiosurgery (SRS) is a feasible approach for patients who are not eligible for liver transplantation or surgical resection [8]; however, randomized clinical trials are still needed to justify its effectiveness. Thermal therapy, such as radiofrequency ablation (RFA), has been regarded as an effective method to control tumor growth with an acceptable morbidity rate [9]. The main advantages of thermal therapy include: 1) minimally invasive with a high safety profile, 2) capability to enable the focal tumor control, 3) favorable long-term survival rate, and 4) it can be combined with other treatment approaches [9].

Despite the promising benefits provided by RFA, it does present some clinical limitations, namely, the precise placement of the RFA needle at the tumor site within the dynamically moving

liver. This has been a long-standing challenge, even with intra-procedural image guidance. Needle targeting error is mainly caused by the respiration-induced movement of the liver, which can be as large as 5.5 cm in the superior-inferior direction [10, 11]. In the manual clinical procedure, errors as much as 7.4 mm in the longitudinal needle-axis direction and 3.6 mm in the lateral direction have been reported [12]. To address this issue, breath-holding is typically required during the placement of the needle to mitigate the motion. However, it can be difficult for patients to hold their breath due to compromised lung capacity and the significant pain associated with the radiofrequency ablation procedure [13]. Even with the advent of modern ventilators to induce active breath control, it is still often more suitable to use free breathing techniques so as to reduce cost and psychological burden to the patient [14, 15]. Many research groups have proposed robotic platforms to assist in needle insertion during percutaneous interventions [16, 17]. These designs can be classified into two categories: 1) the robot only provides needle guidance and 2) the robot has active needle insertion capability. Examples of the first group include the commercially available CT-guided robotic positioning system (ROBIO™ EX, Perfint Healthcare Pvt. Ltd, Florence, OR, USA [18]). Song et al. proposed an MRI compatible double-ring mechanism for MRI-guided liver interventions [19]. A similar platform was reported by Song and Hata for image guided cryotherapy of renal cancer [20]. Hata et al. developed a remote-center-of-motion (RCM) mechanism for MRI-guided microwave therapy [21]. Franco et al. created a 4-DoF robot for MRI-guided laser ablation [22]. A serial robot arm (DLR/KUKA Light Weight Robot III) was used by Tovar-Arriaga et al. to create an FD-CT-guided navigation system for needle placement [23]. Several MRI compatible robotic prototypes have been created by Cleary et al. for percutaneous shoulder arthrography [24, 25] and for treatment of lower back pain [26]. The second group with active needle insertion capabilities is made up of the following. Duan et al. designed a robotic

RCM mechanism on top of a 2-DoF linear slide for RFA of large liver tumors [27]. A robot developed by Stoianovici known as the AcuBot was also used for percutaneous interventions [28]. In addition to these two robots, several autonomous 1-DoF needle insertion robots were developed that focus on the tissue-needle mechanics modeling [29-34]. These robots have shown promise; however, none address the issue of respiration-induced organ motion as most of the accuracy tests were performed in a static phantom or cadaver. Several groups have developed motion prediction algorithms or robot-tissue interaction models to compensate for liver motion, such as the weighted-frequency Fourier linear combiner algorithm [35], iterative learning control method [36], and impedance and admittance control approaches [37, 38]. However, these methods rely on complicated modeling or oversimplified assumptions, thus none have been used in clinical trials to the best of our knowledge.

In this work, we propose the design and evaluation of a novel patient-mounted percutaneous needle insertion robot that mimics the current clinical practice by inserting the RFA needle in accordance with the patient's respiratory motion. This robot is intended to enable accurate ablation needle placement under CT-guidance. Our work is innovative in terms of the 1) active motion compensation protocol, 2) stepwise needle insertion to ensure safety, 3) precise needle position and orientation deployment. These innovations should make our robot safer and more convenient to perform CT-guided RFA for HCC treatment. Our contributions include: (1) the design and modeling of a minimally invasive needle guidance and insertion robot, (2) force modeling of the needle insertion module, and (3) extensive robot validations in static and dynamic phantom and ex-vivo tissue.

2. Methods

2.1. Mechanical Design Overview

The robot consists of three major subsystems: (1) a lower stage with a motorized cartesian carriage, (2) an identical upper stage, and (3) an active needle insertion module that connects both stages together. The upper and lower stages have carriages that are capable of being translated in both x- and y-directions to provide 2-DoF translation. The carriages both have spherical bearings set into them that support the needle insertion module. By changing the relative location between these bearings, 2-DoF orientation of the needle insertion module can be controlled. The needle insertion module provides 1-DoF bidirectional translation of the ablation needle using a custom 3D-printed flexible fluidic actuator. The entire robot is then housed within a 3D-printed Z-frame for the purposes of coordinate frame registration within the CT-scanner [39]. The robot is designed to be mounted directly to the patient to passively compensate for respiratory motion by allowing the robot to move up and down with the patient during periods of respiration. The Z-frame is designed with slots for the placement of adjustable straps to fix the robot according to patient comfort, as seen in the model of the robot in Fig. 1. The adjustable straps allow the robot to be positioned in virtually any position the clinicians deem necessary to reach the target based on preoperative planning. The overall dimensions of the robot are 216 mm × 210 mm × 130 mm with a total weight of 2.17 kg, ensuring a compact design such that the patient can comfortably fit within the CT bore with the robot. Table 1 presents the main robot properties. Note that while this prototype is sufficiently lightweight (less than 3 kg) to ensure patient comfort [40], it is only a proof-of-concept to evaluate the proposed motion compensation protocol. The weight can be further reduced by using lightweight 3D printed pneumatic motors [41] and replacing the metal components with carbon fiber materials.

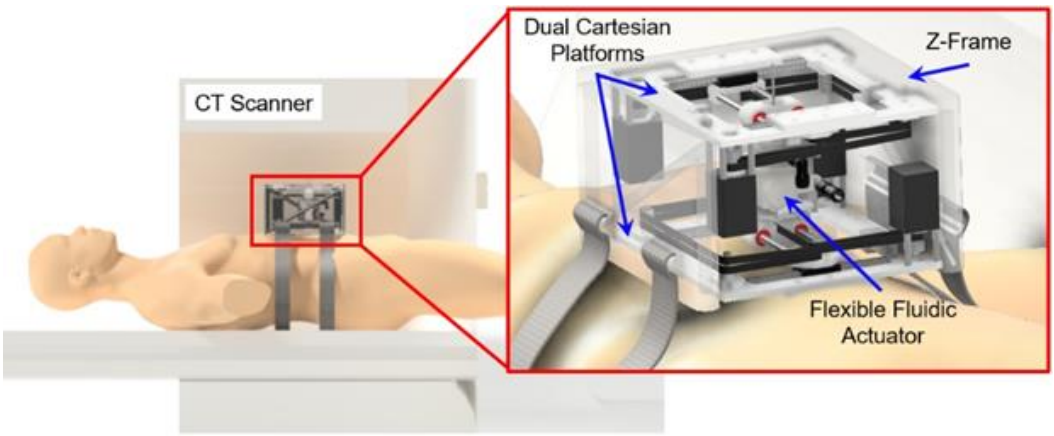

Fig. 1. CAD model of the liver ablation robot mounted on the patient within CT scanner.

Table 1 Robot Properties Based on Design and Workspace Analysis

Robot Dimensions	216 mm × 210 mm x 130 mm
Active DoF	5
x-y Displacement	75 mm x 70 mm
Insertion Depth	Limited by Needle Length
Orientation about x and y axes	± 15°
Weight	2.17 kg

2.2. 4-DoF Cartesian Stages

The upper and lower motorized cartesian stages are based on a custom-designed CoreXY system [42-44], shown in Fig. 2. The system design takes advantage of two statically positioned stepper motors and provides a means of translating both axes independently or simultaneously. The stationary motors have the added benefit of reducing the number of moving parts, increasing the acceleration capabilities of the robot, maintaining a constant center of gravity, and allowing for a more compact design to be implemented.

The carriages are driven by a timing belt attached to the output shafts of four bipolar NEMA 11 stepper motors and the acrylic base frame using friction-reducing pulleys. The motor speeds are limited to 10 mm/s to avoid high accelerations and loss of steps. While these stepper motors are not back drivable under their holding torque, the motion compensation protocol was primarily achieved by the 3D-printed needle insertion module to allow for needle movement in the event of liver motion. Limit switches are used to set the home position of the carriages. Bearing housings, shaft couplers and the carriages themselves are 3D printed using acrylonitrile butadiene styrene (ABS). The low-level control of the cartesian stages is done on a microcontroller (ATmega 2560) with its supporting circuit. The two stages are fixed parallel to each other and held in place by support tabs attached to the fiducial registration Z-frame.

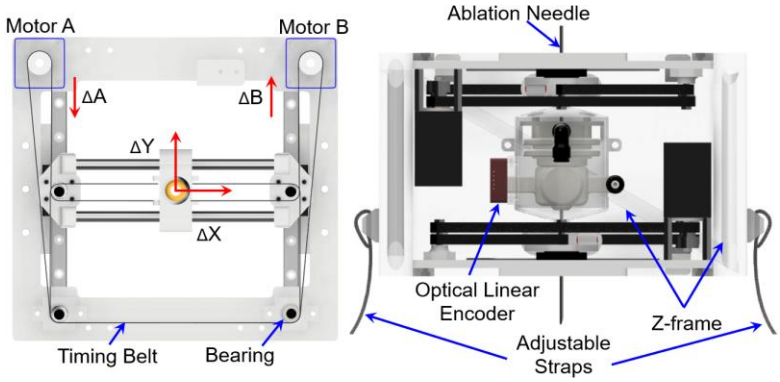

Fig. 2. (Left) CoreXY mechanism of one of the cartesian stages, (Right) CAD model showing the stages connected in parallel via the Z-frame.

2.3. Forward and inverse Kinematics

Inspired by the similarities in dual cartesian platforms as demonstrated by Li et al. in [26], a similar approach to solving the kinematics problems was taken. The coordinate frames, F_{upper} and F_{lower}, for the upper and lower stages are defined identically as being at the center of the spherical bearings in the carriages when both stages are in the homed position as seen in Fig. 3.

The positions of the center of the upper and lower carriages are denoted by $O_{upper} = (x_u, y_u, z_u)$, and $O_{lower} = (x_l, y_l, z_l)$ respectively. The x and y positions of the carriages can be written in terms of the equations of motion governing the CoreXY mechanism that relate motor rotation ΔA and ΔB to translation, given by

$$\Delta x = 1/2\ (\Delta A + \Delta B) \tag{1}$$

$$\Delta y = 1/2\ (\Delta A - \Delta B) \tag{2}$$

The forward kinematics of the robot takes the joint space positions $[x_u, y_u], [\ x_l, y_l]$ along with the desired needle insertion depth, l, and solves for the position of the tip of the needle, in addition to the needle axis vector. The positions of the center of the carriages would then be defined as $O_{upper} = (x_u, y_u, 0)$ and $O_{lower} = (x_l, y_l, -H)$, where H is the constant distance maintained between the two parallel stages of the cartesian platform. The unit vector, $\widehat{N}$, defining the axis of the needle could then be given by the normalized vector of the difference between the positions of the center of the upper and lower carriages. Using this needle axis vector, we can then solve for the position of the of the tip of the needle, $T_{desired}$, using the insertion depth. The equations defining $\widehat{N}$ and $T_{desired}$ are

$$\widehat{N} = \frac{O_{lower} - O_{upper}}{\left\| O_{lower} - O_{upper} \right\|} \tag{3}$$

$$T_{desired} = O_{lower} - l\widehat{N} \tag{4}$$

The robot workspace was simulated in Matlab across the achievable translations in the x- and y-directions of the cartesian stages described previously in Table 1. The blue dots in Fig. 3. show the workspace of the robot and it is overlaid with an average adult human liver. Comparing the volume of the workspace to that of an average adult human liver, the robot can reach 70% of the volume

of an average adult human liver when placed directly above it. Note that the 70% value is just a comparison of the robot workspace to the total size of the average liver.

The inverse kinematics of the robot is used to solve for the joint space positions x_u, y_u, x_l and y_l along with the required needle insertion depth, l, given the desired needle tip position, $T_{desired} = (T_x, T_y, T_z)$, and the needle entry point, $P_{entry} = (P_x, P_y, P_z)$, within the global coordinate frame. The needle vector axis can be defined by

$$N = T_{desired} - P_{entry} \tag{5}$$

Using $N = (N_x, N_y, N_z)$, we can then solve for the positions of the center of the carriages needed to generate this needle axis vector given by,

$$x_u = T_x - \frac{T_z + H}{N_z} N_x \tag{6}$$

$$y_u = T_y - \frac{T_z + H}{N_z} N_y \tag{7}$$

$$x_l = T_x - \frac{T_z}{N_z} N_x \tag{8}$$

$$y_l = T_y - \frac{T_z}{N_z} N_y \tag{9}$$

The insertion depth of the needle, l, is solved for by finding the Euclidean distance between the desired entry point and the location of the desired target,

$$l = \left\| T_{desired} - P_{entry} \right\| \tag{10}$$

In the clinical workflow the point P_{entry} will be defined by the clinician based on pre-operative imaging. The robot forward and inverse kinematics were implemented in a custom Matlab GUI,

whereby $T_{desired}$ and P_{entry} could be input and the coordinates of the upper and lower carriages are solved for to generate the appropriate needle vector axis. These joint space positions in addition to the needle insertion depth are then communicated to the robot over a serial bus to the low-level microcontroller such that the robot can be aligned to the desired location.

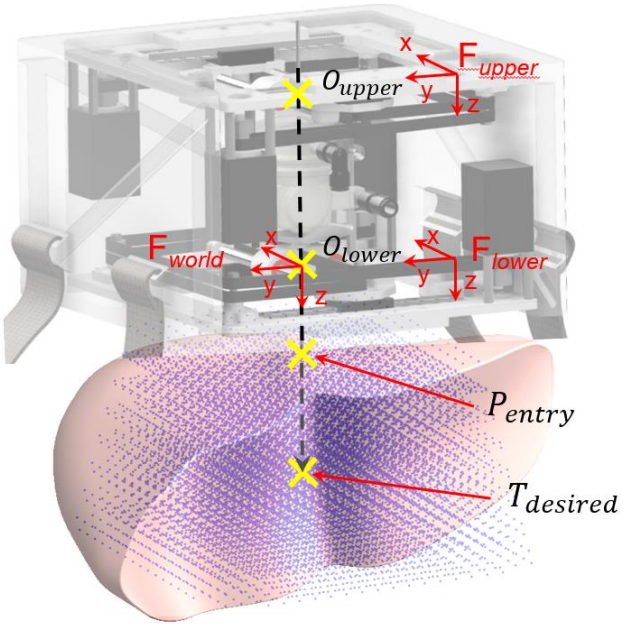

Fig. 3. Coordinate frame assignment of the patient mounted robot. Forward kinematics indicates that the robot workspace (blue point cloud) is able to cover 70% of the liver.

2.4. Active Needle Insertion Module

The active needle insertion module utilizes a modified, more compact design based on an MR-compatible needle driver developed by Comber et al. [45]. The modifications made include: 1) The needle insertion module dimension has been significantly reduced from Φ 8.9 cm $\times$ 33 cm to Φ 5.8 cm $\times$ 7 cm such that the robot can be operated within the CT scanner. This is achieved by using only 2 linear bellows, using a single gripper, and eliminating the rotation bellow, and 2)

The insertion force was theoretically modeled and experimentally validated in order to guarantee that the design could generate the forces necessary to penetrate tissue. The design consists of two key components that allow for 1-DoF needle translation: (1) the linear bellow actuator and (2) the gripper. The mechanism is also referred to as a flexible fluidic actuator (FFA) since both components are actuated using pressurized air. The linear bellow actuator consists of a toroidal bellow geometry such that the hollow center can be used to translate the needle through the device's central axis. Under operation, the needle can be grasped using the gripper mechanism, which consists of two flat diaphragms that when inflated, expand to grasp the needle. The FFA, seen in Fig. 4a, was 3D printed in the material nylon-12 using selective laser sintering (SLS). Safety tabs (see Fig. 4b) were added to the design to restrict the linear translation of the mechanism to < 2mm. The concept of safety tabs is crucial to ensure safe operation of the device to within only one full step of the FFA in the event of a system failure. The FFA is housed within a 3D printed housing, as seen in Fig. 4b, that consists of mechanical stop brackets to restrict the linear displacement of the FFA to a step size of 1.5 mm. Attached to the housing is an optical encoder (US-Digital part no. EM1-1-500-N), and a linear transmissive strip (500 lines per inch) is mounted to the safety tab on the FFA. This is done so that the relative displacement between the housing and FFA could be measured to determine the insertion or retraction depth of the needle. The FFA was controlled using two proportional directional control valves (Festo MPYE-5-M5-010-B) with the control signal supplied via a microcontroller (ATmega 2560) and amplifier circuit.

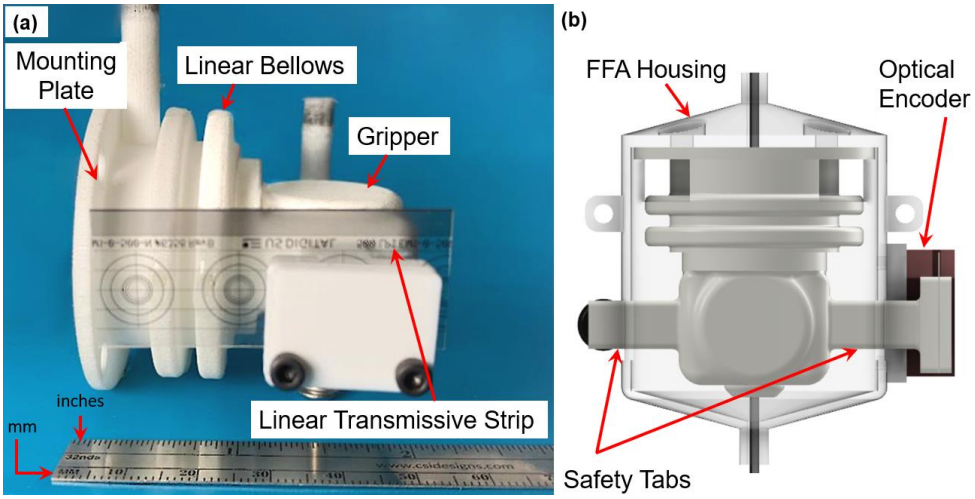

Fig. 4. (a) SLS 3D printed flexible fluidic actuator with attached linear transmissive strip, (b) CAD model of the flexible fluidic actuator, its housing with mounted linear optical encoder

2.5. Active Motion Compensation Protocol

An active motion compensation protocol is proposed for operating the patient mounted robot. In this protocol, the ablation needle will be automatically deployed towards the liver tumor during the stationary phase of the respiration cycle. The stepwise "move-pause" insertion protocol is inspired by the manual insertion procedure, whereby the clinician typically inserts the needle when the liver has the least motion and releases the needle when respiration induced motion is significant. The respiratory cycle of the patient will be gated using the GE D690 PET/CT scanner which uses the Varian CT Real-Time Position Management system (Varian Medical Systems, Palo Alto, CA). The Real-Time Position Management system consists of reflectors attached to an external marker placed on the patient's abdomen [46]. The marker motion reflects the breathing pattern of the patient and can be captured by an external camera at a frequency of 30 Hz [47] to obtain a surrogate respiratory signal. The system is able to track the real-time position data even when the respiratory rate changes suddenly. The needle insertion module must complete a full-step insertion when the liver has negligible movement in its static phase and release the needle

when the liver undergoes significant movement during its dynamic phase. In order to achieve this protocol, the insertion sequence is divided into four sequential steps: grasp, insert, release, and home. Fig. 5a shows the finite element method (FEM) simulation of the FFA motion subject to the pressure input. Retracting the needle can be achieved by alternating the sequence to power the FFA. Note that the operation process must be completed within about 2s to cover just the static phase as seen in Fig. 5b. The current prototype of the needle insertion module is capable of inserting the needle at a maximum speed of 1.5 mm/s.

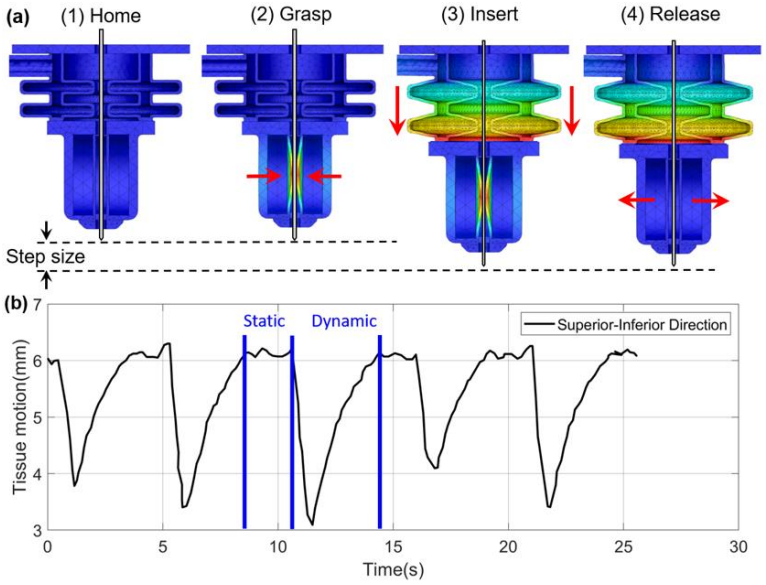

Fig. 5. (a) Illustration of the sequential step-like grasp-insert-release method of actuation of the needle insertion module. The linear bellow will be depressurized to the home position after the release step. (b) static and dynamic phases of an in-vivo porcine liver

2.6. Robotic RFA Clinical Workflow

In the proposed clinical workflow, the patient will be positioned in the GE D690 PET/CT scanner and the robot will be fixed to the patient's abdomen using adjustable straps. An initial CT scan will be performed to register the robot to the CT scanner using the point-based registration method [44]. A second CT scan will be used to identify the desired target location, which will be

used by the radiologist to determine an appropriate needle entry point. The robot will automatically align the needle insertion module to the desired target and the needle can then be progressed towards the ablation target. During the needle insertion process, the Varian CT Real-Time Position Management system will continuously track the patient's respiratory cycle. According to the proposed motion compensation protocol, the needle is only advanced when the liver has the least amount of motion (static phase, see Fig. 5b). Once the needle is placed at the target location, a confirmation scan will be conducted to verify the needle location, and ablation therapy will then be performed. The detailed workflow is shown in Fig. 6.

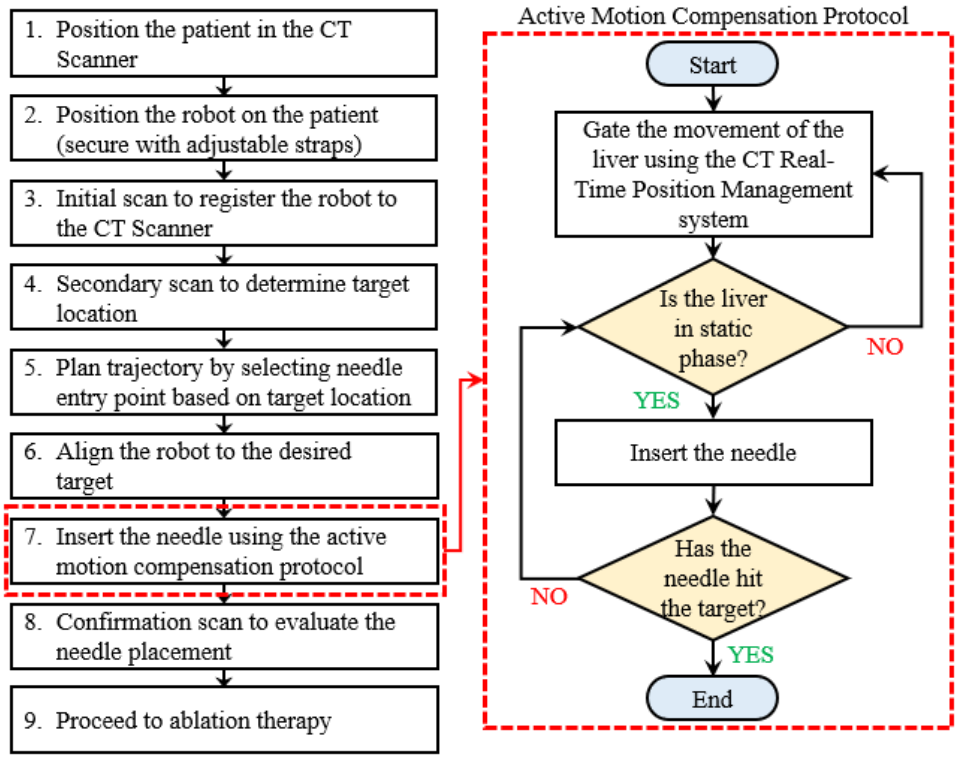

Fig. 6. The proposed clinical workflow of the robot

2.7. Force Modeling of the Needle Insertion Module

In this section, we focus on the force modeling of the FFA to estimate the force the FFA is capable of inserting a needle with. According to [48], the axial force of the linear bellows, F_A , is given by,

$$F_A = \pi(R + h)^2 x P \tag{11}$$

$$x = \frac{(1 - \rho^2)(1 - \rho^4 + 4\rho^2 \ln \rho)}{4(1 - \rho^2 + 2\rho \ln \rho)(1 - \rho^2 - 2\rho \ln \rho)} \tag{12}$$

$$\rho = \frac{R - h}{R + h} \tag{13}$$

The parameter R defines the mean radius of the bellow, and h is half the wave height of a corrugation, as depicted in Fig. 7. In addition to this axial force caused by the linear bellows, the force of friction that the gripper is holding the needle with plays a key role in determining the needle insertion force and should be considered. From a review of the principles from mechanics of materials [49], the deflection of a thin circular plate with clamped outer edges and a free inner edge is given by

$$y_{max} = \frac{P a^4}{64 D} \tag{14}$$

where P is a uniformly distributed pressure over the surface area of the diaphragm, a is the radius of the diaphragm, and D is the flexural rigidity defined in (15) as

$$D = \frac{E t^3}{12(1 - \nu^2)} \tag{15}$$

where E and ν are the material properties Young's modulus and Poisson's ratio, respectively, and t is the thickness of the diaphragm. Again, from mechanics of materials, we can derive the normal force, F_N, acting on the needle due to the deflection of the diaphragms. The relationship between the normal force and the displacement at the center of the diaphragm is given by,

$$y_{max} = \frac{F_N a^2}{16\pi D} \tag{16}$$

Substituting (14) and (15) into (16) we then have a relationship between the input internal pressure of the diaphragm chamber and the normal force generated between the diaphragms and the needle. A scaling factor of 2 is included since the normal force is being applied to both sides of the needle. This relationship is given by,

$$F_N = \frac{\pi}{2} P a^2 \tag{17}$$

Using this normal force to pressure relationship, we can then estimate the force of friction holding the needle in place by multiplying the normal force by the coefficient of friction, 0.35, of the material. For an input pressure of 345 kPa, an estimated 24.6 N of friction force will be used to clamp onto the needle. This force is considered as more than sufficient for percutaneous needle interventions [50-52].

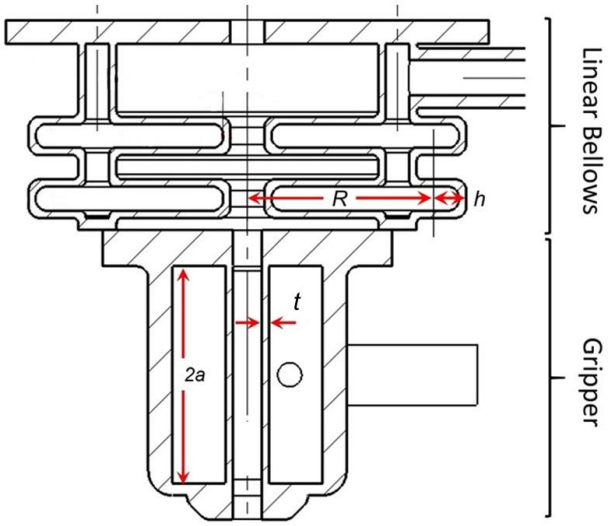

Fig. 7. Parameters used in force estimation and analysis

3. Experiments and Results

Several experiments were conducted to characterize the performance of the robot: a) free-space accuracy evaluation of the 4-DoF dual cartesian stages, b) free-space accuracy and repeatability of the needle insertion module, c) force characterization of the needle insertion module, d) static phantom and static ex-vivo porcine liver tissue targeting, e) dynamic phantom targeting, and f) dynamic ex-vivo porcine liver tissue targeting.

3.1. Accuracy analysis of the dual cartesian stages

To characterize the accuracy of the dual cartesian stages, a free-space analysis was conducted. This was done using the Aurora electromagnetic (EM) tracking system (NDI Medical, Ontario, Canada) with resolution of 0.5 mm. The two carriages were linked together, allowing the central axis between the two carriages to be more easily identified. A 5-DoF EM sensor was used to track the position of the central axis between the carriages. Coordinate registration was done to be able to track the sensor within the robot reference frame using the point-based registration method [53]. The reference frame registration was taken after initially homing both stages of the

robot. From there, a desired path was sent to the robot via the Matlab GUI and the real time position was tracked. The desired paths consisted of four squares of length 10 mm, 20 mm, 30 mm, and 40 mm, all created by streamlining the coordinates of the corners of the square to the GUI as seen in Fig. 8. The mean error across three experiments for each desired path was measured at the corners of the squares in both the x- and y-directions. The mean error in the x-direction is 0.18 ± 0.18 mm and the mean error in the y-direction is 0.32 ± 0.23 mm. These free-space experimental results were taken as validation for sufficient accuracy of the dual cartesian system to potentially be used for precise needle placement operations.

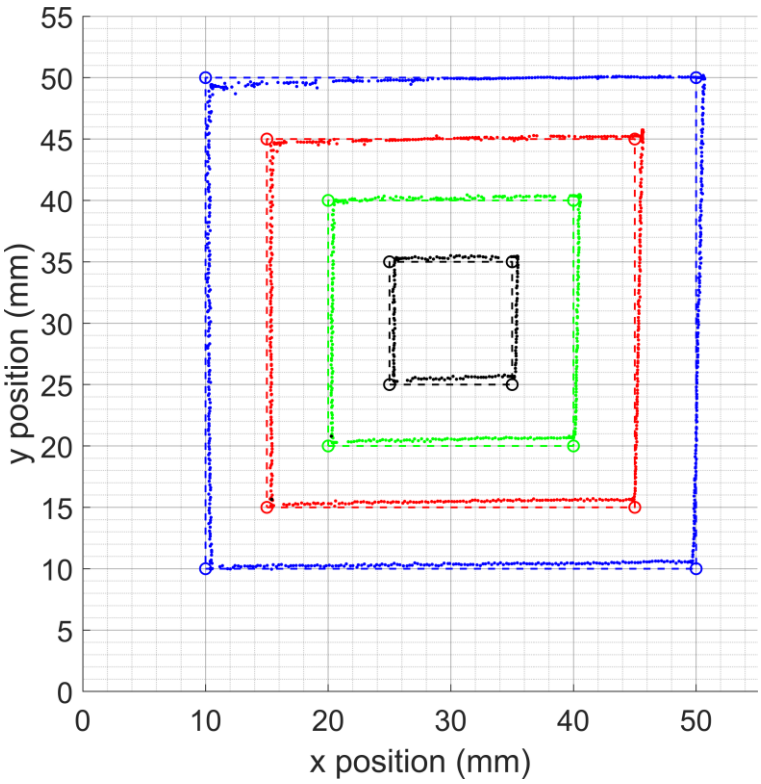

Fig. 8. Desired path versus the actual tracked path of the Cartesian stages. The dashed lines represent the desired path while the dots show the data collected from the EM tracker

3.2. Accuracy and Repeatability of needle insertion module

To characterize the accuracy of the needle insertion module, the EM tracker was again used to perform insertion in free space. An EM sensor was attached to the tip of a needle and a custom 3D printed bracket was used for coordinate registration. The needle used was an 18-gauge needle with diamond shaped tip. Eight insertion depths of 15 mm, 30 mm, 45 mm, 60 mm, 75 mm, 90 mm, 105 mm and 120 mm were sent to the needle insertion module from the GUI for a total of three iterations for each depth. The error was considered to be the difference between the measured insertion depth and the desired depth. The mean error across all 24 experiments was found to be 0.64 ± 0.38 mm (see Table 2 for the error results at each insertion depth). Note that the error does not accumulate as the needle insertion depth is increased due to the step-wise operation of the needle insertion module. This step-wise insertion ensures that the needle insertion error is within one full step-size of the FFA (1.5 mm). The repeatability of the needle insertion module was quantified by evaluating the Coefficient of Variation (CV) [41, 54]. The CV is expressed as a percentage, and the lower the percentage, the better the repeatability is. The results of the needle insertion experiment are presented in Table 2.

Table 2 Needle Insertion Accuracy and Repeatability

Desired Insertion Depth (mm)	Mean Measured Depth (mm)	|Mean Error| (mm)	STD of the Measured Depth (mm)	CV %
15	15.94	0.94	0.10	0.62
30	30.49	0.49	0.19	0.61
45	44.97	0.23	0.25	0.55
60	60.26	0.84	0.80	1.33
75	76.12	1.12	0.51	0.67
90	90.40	0.56	0.49	0.54
105	105.17	0.56	0.54	0.51
120	120.16	0.36	0.43	0.36
Mean		0.64	0.38	0.65

3.3. Force characterization of needle insertion module

In addition to the insertion testing accuracy in free-space, the forces generated by the FFA were also characterized. The insertion force due to pressurizing the linear bellows was found by placing a force sensor (Vernier Go Direct® Force and Acceleration Sensor) with a flat plate adapter directly against the FFA as seen in Fig. 9(a). The pressure inside the linear bellows was slowly increased from 0 kPa to 110 kPa, corresponding to the maximum force measurable by the force sensor. As the pressure was increased, the insertion force was recorded at intervals of 17.5 kPa (2.5 psi). A custom 3D printed bracket was designed to attach the safety tabs on the FFA to the force sensor. It was configured such that the linear bellows could be pressurized and allow the pulling, retraction force of the bellows to be measured as they were depressurized, as seen in Fig. 9(b). As the pressure was decreased, the corresponding retraction force was recorded for the same intervals as previously mentioned. The results of the linear bellows force characterization were compared to the predicted forces calculated using (11) - (13) in Section II-C as seen in Fig. 10(a) and (b). A mean error of 2.57 ± 0.6 N was found for the insertion force experiment and a mean error of 4.04 ± 1.39 N was found for the retraction force experiment. . These errors can be largely attributed to manufacturing imperfections in the FFA.

The linear bellows are capable of producing significantly more force than the gripping diaphragms at the same pressure input, therefore we expect the needle to slip between the diaphragms at a certain point. To characterize this frictional force, the FFA was set up as seen in Fig. 9(a), but rather than having the force sensor pressed up against the FFA, a needle was placed between the grippers at 345 kPa and the force sensor then positioned at the tip of the needle. The pressure inside the linear bellows was then increased and the force at the tip of the needle was monitored. A noticeable peak force was achieved which corresponded to the needle beginning to

slip due to the change from static friction to dynamic friction, as seen in Fig. 10(c). Based on the calculations in Section II-C a peak force of 24.6 N was expected, while the experimental results indicate a mean peak force of 22.6 ± 0.40 N across three trials. This difference of 8.4% may be as a result of manufacturing imperfections and environmental conditions affecting the coefficient of friction between the two materials. The linear bellows force characterization and the friction force analysis both indicate more than sufficient force is achievable to perform percutaneous liver interventions, where a peak force of about 6 N was recorded for the percutaneous interventions based on previously mentioned research.

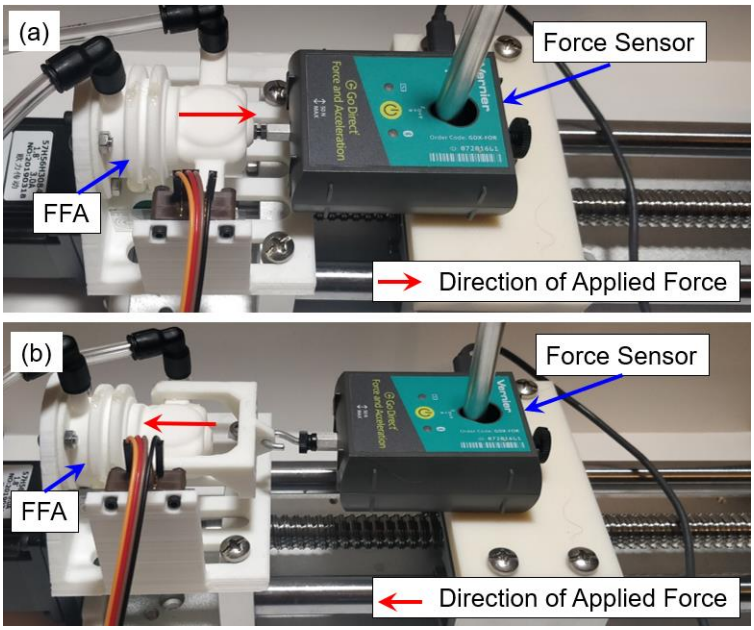

Fig. 9. Experimental setup for the linear bellows characterization, (a) characterization of the FFA insertion force, (b) characterization of the FFA retraction force

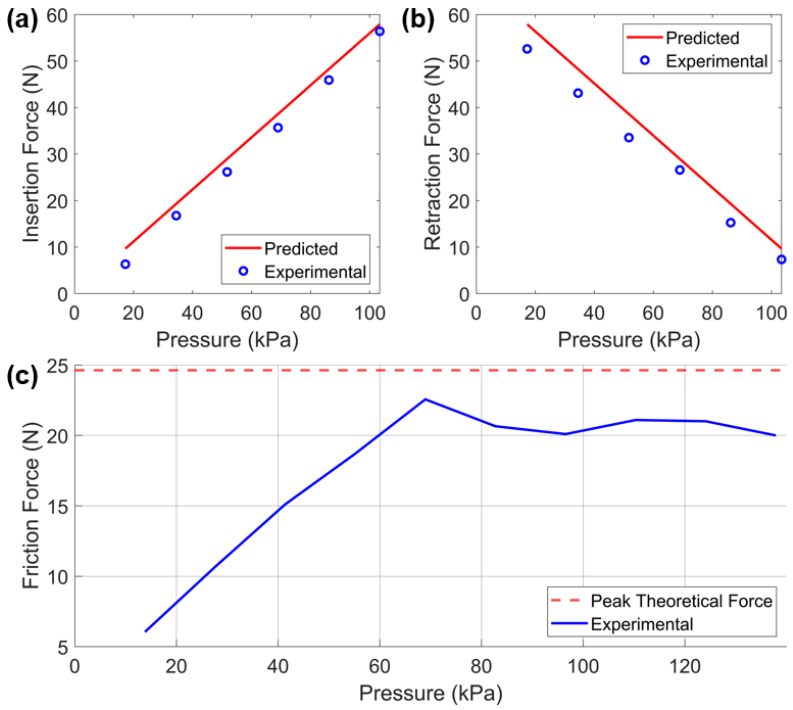

Fig. 10. Results of the FFA characterization: (a) insertion force characterization results, (b) retraction force characterization results, (c) experimental friction force between the gripper and the needle as the pressure input to the linear bellows is increased compared to the theoretical peak friction force with the pressure input of 345 kPa to the gripper mechanism.

3.4. Robot Targeting Test: Static phantom and ex-vivo porcine liver trial

A 5% by volume agar gelatin phantom was created to mimic soft liver tissue. The experiment was conducted by selecting 24 arbitrary points, grouped into four groups of 6 points, within the robot's workspace and using their xy-location as the desired target. For the first group of six points, the desired insertion depth was increased from 15 to 90 mm in 15 mm increments across the points and the needle orientation was set to 0°. This was then repeated for the remaining three groups however the needle orientation about the x-axis was increased in 5° increments across the groups. Using these values as the desired input to the robot GUI, the needle was placed and automatically deployed to the phantom via the needle insertion module. The final location of the needle was recorded by the EM tracker. Each targeting experiment was conducted three times and

the mean values were used in quantifying the accuracy of the robot. The positional error was defined to be the Euclidean distance between the desired target and the measured location. Additionally, the orientational error is defined by the difference between the desired input angle and the measured angle. The results for the static phantom experiment show that there is a mean positional error of 1.14 ± 0.30 mm and an orientational error of 0.99° ± 0.36°.

The same points and grouping scheme were used to repeat the experiment in a static ex-vivo porcine liver except the insertion depth increased from 10 to 60 mm in increments of 10 mm, where 60mm was the maximum thickness of the porcine liver sample used. Porcine liver has often been used to mimic an environment for testing needle insertion devices in place of human tissue. The porcine liver was acquired fresh from a local meat supplier, and prior to testing the liver was allowed to come to room temperature. The results show that there is a mean positional error of 1.22 ± 0.31 mm and an orientational error of 1.16° ± 0.44°. A top view of the static targeting experiments can be seen in Fig. 11. There is a slight increase in positional targeting error of the needle with respect to the insertion depth in both the static phantom and ex-vivo liver trials. This can be seen in Fig. 12 where there is a general increasing trend in the positional error as the insertion depth is increased. The targeting error, however, does not show any significant statistical relation to the increasing inclination of the needle.

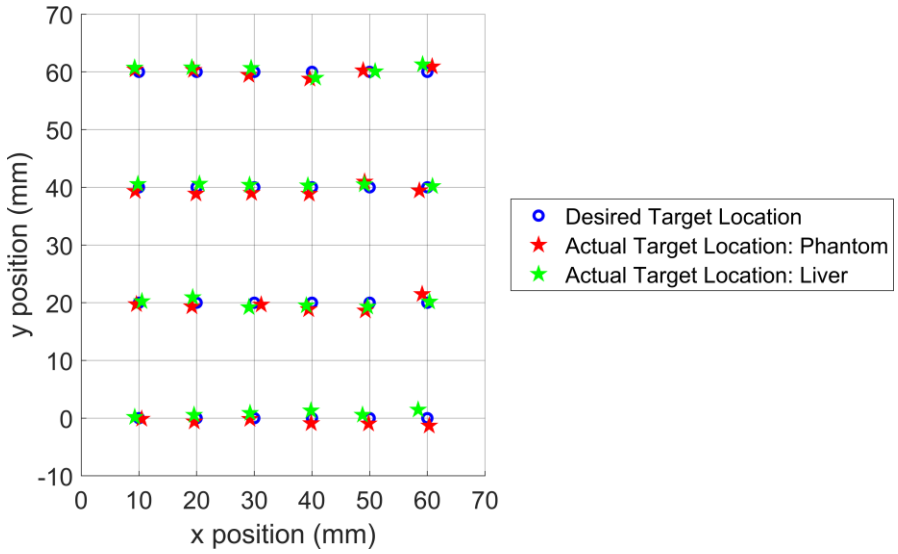

Fig. 11. Top view of the static targeting experiments. The blue circles represent the desired target location, the red stars show the measured needle position in the static phantom, and the green stars show the measured needle position in the static ex-vivo porcine liver.

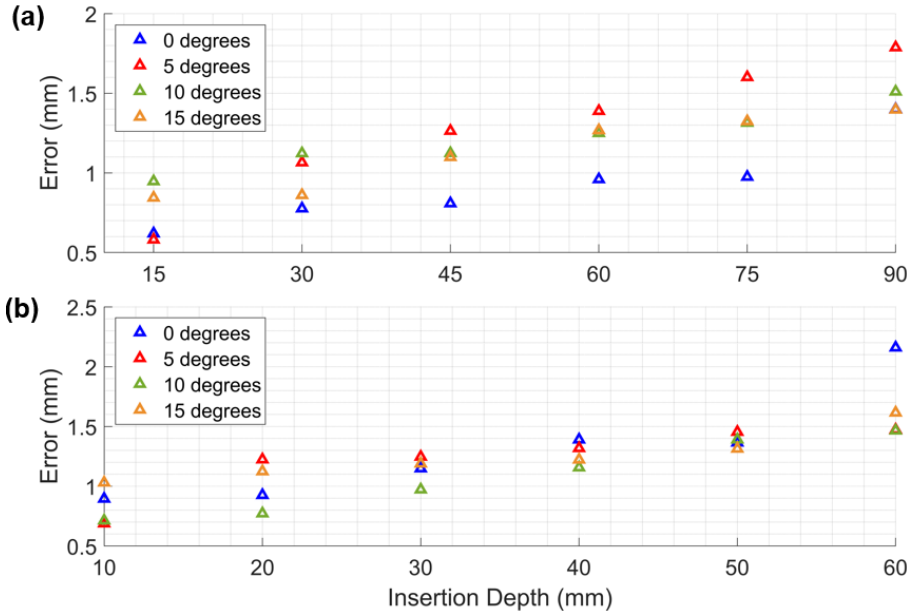

Fig. 12. (a) Static phantom needle targeting error vs. insertion depth (b) Static ex-vivo porcine liver needle targeting error vs. insertion depth. In both tests, the needle insertion angle was increased from 0° to 15° in increments of 5°.

3.5. Robot targeting: Dynamic phantom trial

To validate the robot's targeting performance under the dynamic conditions of the liver, a dynamic motion platform was developed to create a relative displacement between the robot and the phantom. The motion platform consists of two stepper motor driven linear rails fixed to one another perpendicularly in the horizontal plane as seen in Fig. 13. A two-dimensional dynamic phantom was chosen rather than considering three-dimensional motion for two primary reasons. Based on our previous research [55], liver motion in the inferior-superior (I-S) and left-right (L-R) is dominant in comparison to the motion generated in the posterior-anterior (P-A) direction (~ 1.2 mm). A two-dimensional dynamic motion platform also greatly simplified the robotic motion platform, especially during the prototype characterization period. Between every two steps of the needle insertion process, the motion platform moves the phantom 10mm in the x-direction and 5mm in the y-direction to simulate the respiratory induced motion of the liver in the I-S direction and L-R direction, respectively. While the phantom is in motion, the needle insertion module releases the needle to allow it to move with the phantom freely. Once the platform has returned to its original position, the needle insertion module takes another two full insertion steps and the process is repeated until the needle has reached its final target. The stepwise "move-pause" insertion protocol is inspired by the manual insertion procedure, where the clinician typically inserts the needle when the liver has the least motion and releases the needle when respiration motion is significant. Twenty-four targets were selected by arbitrarily inserting the 6-DoF EM tracking probe (NDI Medical, Ontario, Canada) into the phantom. The location of the target, the tip of the EM tracking probe, was then converted into the robot frame and used as an input for the GUI. Similar to the static phantom trial, the 24 points were grouped into 4 groups of 6 and the desired insertion depth of the needle was user controlled from 15 to 90 mm in 15 mm increments

while the needle orientation across each group was increased from 0° to 15° in increments of 5°. Three insertion trials were conducted for each target and the error for these dynamic targeting experiments is defined to be the same as in the static experiments. The results of the dynamic targeting experiments in phantom indicate a mean positional error of 1.69 ± 0.66 mm and a mean orientational error of 1.66 ± 0.50°.

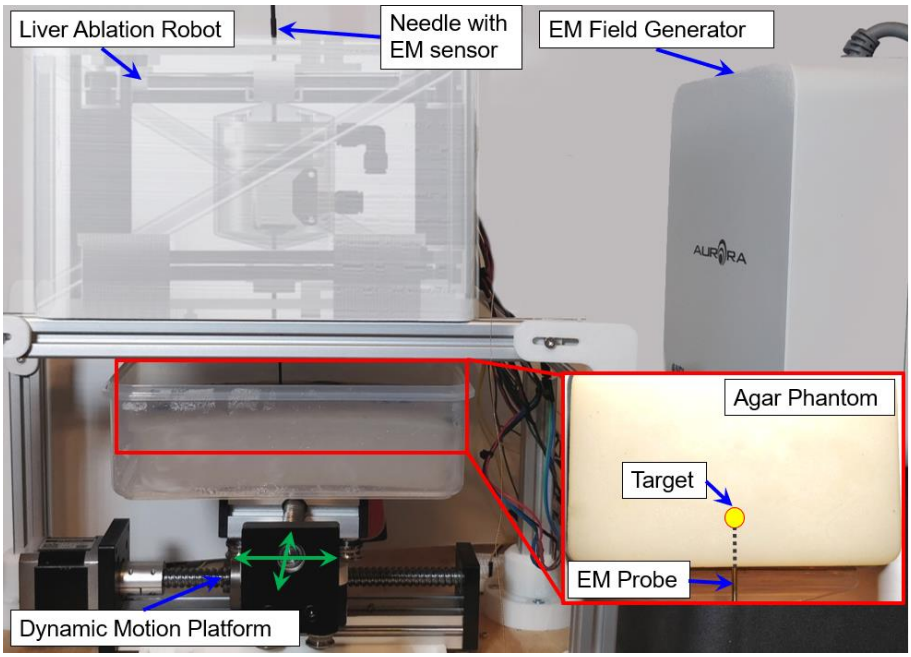

Fig. 13. Experimental setup of the dynamic phantom experiments. The green arrows indicate the directions of motion of the platform that creates the 2-DoF translation of the phantom. The CAD model of the robot is overlaid on the image for clarity.

The dynamic targeting experiments were repeated, however, this time no motion compensation was considered. The synchronicity between the needle insertion module and the motion platform was disabled so that there was no consideration of the location of the moving target with respect to the insertion of the needle. The needle was inserted with constant speed until it reached its final target, the motion platform was simultaneously stopped, and the final needle position was recorded. The results of this dynamic targeting experiment with no motion

compensation indicates a mean positional error of 5.02 ± 2.35 mm and a mean orientational error of 4.54 ± 1.40°. A comparison between the dynamic phantom targeting experiments with active motion compensation and without motion compensation is shown in Fig. 14.

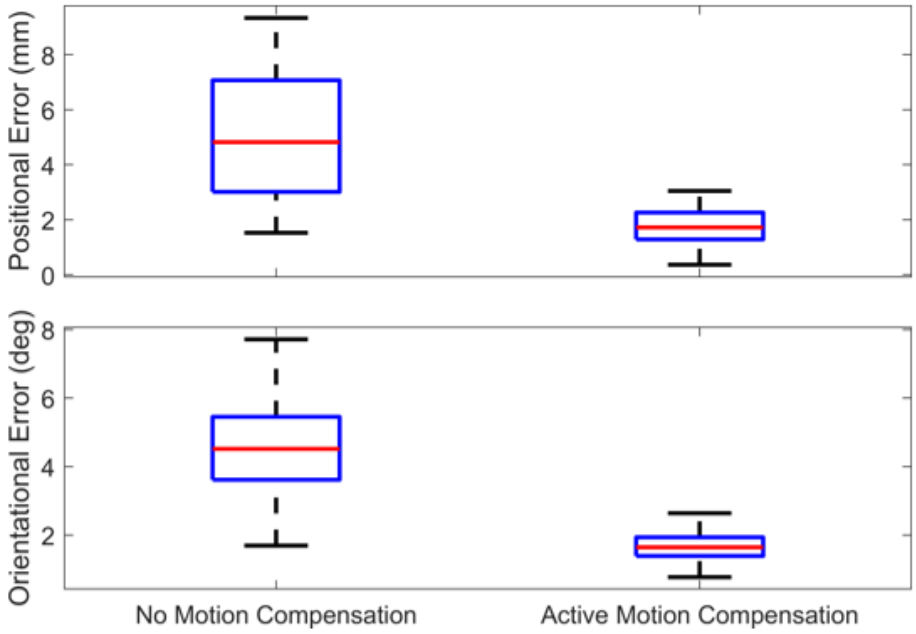

Fig. 14. Comparison of dynamic phantom targeting experiments with and without active motion compensation

3.6. Robot targeting: Dynamic ex-vivo porcine liver trial

To simulate targeting in biological tissue, an ex-vivo porcine liver sample was used in place of the agar phantom. The same workflow used in the dynamic phantom targeting experiments was employed here for a total of 24 targets. With the motion compensation protocol implemented, the results indicate a mean positional error of 1.54 ± 0.55 mm and a mean orientational error of 1.68 ± 0.47°. The experiments were repeated without the motion compensation protocol implemented and the results show a mean positional error of 5.07 ± 2.44 mm and a mean orientational error of 4.06 ± 1.45°. A comparison of these results is presented in Fig. 15. Similar to the static

experiments, a slight increase in positional targeting error was observed in both the phantom and ex-vivo liver trials, more noticeably in the ex-vivo liver as seen in Fig. 16. Again, no noticeable statistical correlation could be made between targeting error and increasing inclination of the needle.

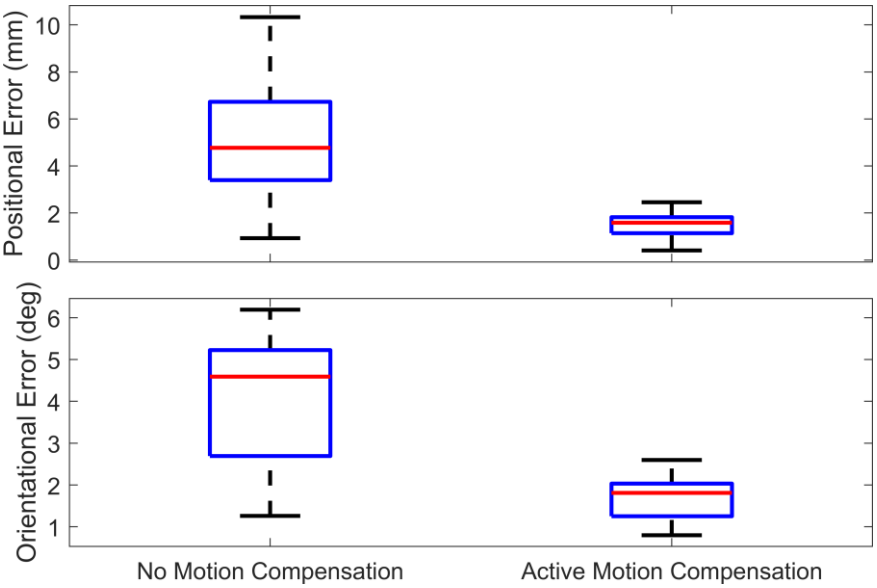

Fig. 15. Comparison of ex-vivo porcine liver dynamic targeting experiments with and without active motion compensation

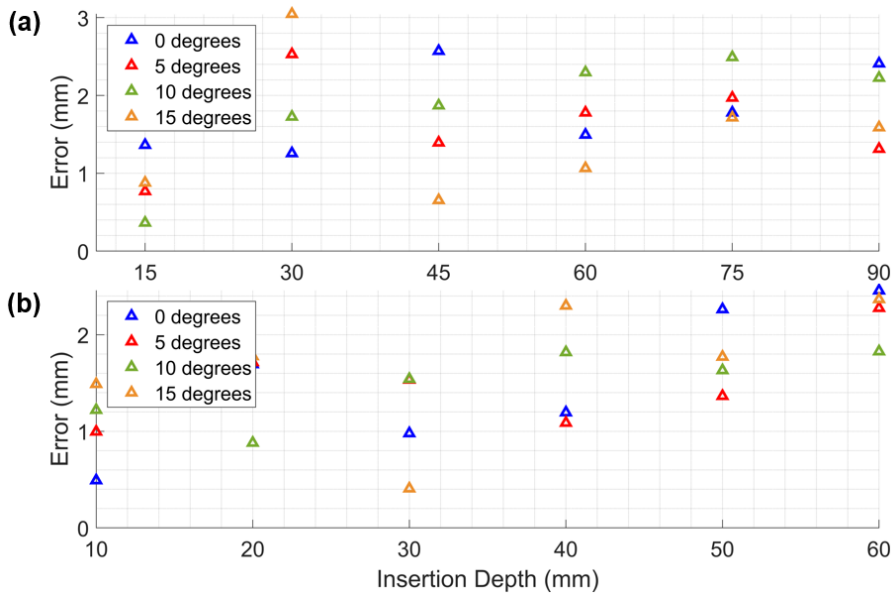

Fig. 16. (a) Dynamic phantom needle targeting error vs. insertion depth (b) Dynamic ex-vivo porcine liver needle targeting error vs. insertion depth. In both experiments, the needle insertion angle was increased from 0° to 15° in increments of 5°.

4. Discussion and Conclusion

This paper presents the design, fabrication, and preliminary benchtop characterization of a 5 DoF, patient mounted robot to perform percutaneous needle interventions for the treatment of hepatocellular carcinoma. The robot includes a dual cartesian platform with a custom 3D printed active needle insertion module and is designed to be directly mounted onto the patient's abdomen. With the step-wise needle insertion module, an active motion compensation protocol is proposed to further reduce any targeting errors that may be caused by the respiratory induced motion of the liver.

The system was first analyzed on an individual subsystem level to validate the accuracy of that specific component before moving on to complete system testing. In free-space testing, the accuracy of the dual cartesian platform was shown to have a mean error of 0.18 ± 0.18 mm in the x-direction, and a mean error of 0.32 ± 0.23 mm in the y-direction. Additionally, in free-space

testing, the needle insertion module demonstrated needle insertion accuracy of 0.64 ± 0.38 mm mm along the axis of the needle, with good repeatability indicated by an average CV of 0.65%. Force characterization experiments showed sufficient force generation from the needle insertion module to perform percutaneous needle interventions. The submillimeter accuracy of these two metrics and the force requirement being met was taken as validation of the main subsystems and warranted further analysis of the robot.

In the static phantom targeting experiments, the mean positional error was demonstrated to be 1.14 ± 0.30 mm, and the mean orientational error was found to be 0.99 ± 0.36°. Additionally, in the static ex-vivo liver targeting experiments, the mean positional error was demonstrated to be 1.22 ± 0.31 mm, and the mean orientational error was found to be 1.16 ± 0.44°. This served as a benchmark for the dynamic targeting experiments. In the next stages of testing, the dynamic motion of the liver was simulated by a phantom mounted to a dynamic platform. Using the protocol of only inserting the needle during the stationary period of the phantom's trajectory gave similar results to the static phantom experimentation with mean positional error of 1.69 ± 0.66 mm and mean orientational error of 1.66 ± 0.50°. This was then compared to experiments that did not consider the motion compensation strategy where there is noticeably large variance in the results and high positional error and orientational error. We see a 66.3% improvement in positional accuracy when the active motion compensation protocol is implemented versus when it is not. The dynamic experiments were once again repeated, however in an ex-vivo porcine liver to recreate insertion into biological tissue. The results of this experiment show a mean positional error of 1.54 ± 0.55 mm and a mean orientational error of 1.68 ± 0.47°. Similar to the dynamic phantom experiments, with the motion compensation protocol implemented the results showed a 69.6% improvement in positional accuracy over those trials that did not implement the motion

compensation protocol. The lack of active motion compensation gave way to high variance, high positional and high orientational errors.

The errors seen in these experiments can be attributed to fabrication deviations and registration errors. Manufacturing errors lead to misalignment of the upper and lower Cartesian stages, and while calibration measures were taken to account for this, other sources of errors may have arisen from backlash in the timing belts, and flexion in the acrylic and 3D printed components. Additional fabrication errors can be attributed to the deviations seen between the force characterization experiments and the predicted values. Improvements could be made to minimize errors in fabrication such as using high precision machined components rather than 3D printed parts and leadscrews with anti-backlash systems in place. Closed-loop motors could also be used to account for losses in steps.

The implementation of a robotic platform as proposed in this study could potentially lead to the safer and more efficient treatment of HCC. This first characterization study serves as a critical first step to providing precise needle placement within the dynamic environment of the abdominal region. In future work, radiolucent and more lightweight materials such as carbon fiber rods and 3D printed pneumatic motors will be used in place of the metallic components used in this current prototype. To increase the workspace of the robot by allowing for greater inclination of the needle insertion module, custom spherical bearings will be used in future iterations of this robotic platform. Additionally, a haptic feedback master device will be developed to allow the clinician to sense the needle insertion forces throughout the procedure. Further work will be done to analyze the robot's performance within the CT Scanner, to implement closed-loop control with CT Real-Time Position Management feedback and to evaluate the robot's performance in animal trials.

5. References

[1] A. C. Society, "Key Statistics About Liver Cancer," ed, 2020.

[2] H.-s. Kim and H. B. El-Serag, "The Epidemiology of Hepatocellular Carcinoma in the USA," Current Gastroenterology Reports, vol. 21, no. 4, p. 17, 2019/04/11 2019.

[3] L. G. Mantovani and M. Strazzabosco, "Healthcare costs associated with hepatocellular carcinoma and the value of care," Hepatology, vol. 58, no. 4, pp. 1213-1214, 2013/10/01 2013

[4] J. M. Llovet et al., "Sorafenib in Advanced Hepatocellular Carcinoma," New England Journal of Medicine, vol. 359, no. 4, pp. 378-390, 2008/07/24 2008, doi: 10.1056/NEJMoa0708857.

[5] S. Daher, M. Massarwa, A. A. Benson, and T. Khoury, "Current and Future Treatment of Hepatocellular Carcinoma: An Updated Comprehensive Review," Journal of clinical and translational hepatology, vol. 6, no. 1, pp. 69-78, 2018.

[6] A. Z. Azzam, "Liver transplantation as a management of hepatocellular carcinoma," World journal of hepatology, vol. 7, no. 10, pp. 1347-1354, 2015.

[7] R. Wong and C. Frenette, "Updates in the management of hepatocellular carcinoma," Gastroenterology & hepatology, vol. 7, no. 1, pp. 16-24, 2011.

[8] K. Goyal et al., "Cyberknife stereotactic body radiation therapy for nonresectable tumors of the liver: preliminary results," HPB Surgery, vol. 2010, 2010.

[9] H. Rhim and H. K. Lim, "Radiofrequency ablation of hepatocellular carcinoma: pros and cons," Gut and liver, vol. 4 Suppl 1, no. Suppl 1, pp. S113-S118, 2010.

[10] B. Bussels et al., "Respiration-induced movement of the upper abdominal organs: a pitfall for the three-dimensional conformal radiation treatment of pancreatic cancer," Radiotherapy and Oncology, vol. 68, no. 1, pp. 69-74, 2003.

[11] I. Suramo, M. Päivänsalo, and V. Myllylä, "Cranio-caudal movements of the liver, pancreas and kidneys in respiration," Acta radiologica. Diagnosis, vol. 25, no. 2, pp. 129-131, 1984.

[12] G. Widmann, P. Schullian, M. Haidu, M. Fasser, and R. Bale, "Targeting accuracy of CT-guided stereotaxy for radiofrequency ablation of liver tumours," Minimally Invasive Therapy & Allied Technologies, vol. 20, no. 4, pp. 218-225, 2011/07/01 2011.

[13] R. Poon et al., "Learning curve for radiofrequency ablation of liver tumors: prospective analysis of initial 100 patients in a tertiary institution," Annals of surgery, vol. 239, pp. 441-9, 05/01 2004.

[14] Q. J. Wu, D. Thongphiew, Z. Wang, V. Chankong, and F.-F. Yin, "The impact of respiratory motion and treatment technique on stereotactic body radiation therapy for liver cancer," Medical Physics, vol. 35, no. 4, pp. 1440-1451, 2008/04/01 2008.

[15] R. Li, W. Si, X. Liao, Q. Wang, R. Klein, and P.-A. Heng, "Mixed reality based respiratory liver tumor puncture navigation," Computational Visual Media, vol. 5, no. 4, pp. 363-374, 2019/12/01 2019.

[16] M. M. Arnolli, N. C. Hanumara, M. Franken, D. M. Brouwer, and I. Broeders, "An overview of systems for CT- and MRI-guided percutaneous needle placement in the thorax and abdomen," International Journal of Medical Robotics and Computer Assisted Surgery, Review vol. 11, no. 4, pp. 458-475, Dec 2015

[17] J. Kettenbach and G. Kronreif, "Robotic systems for percutaneous needle-guided interventions," Minimally Invasive Therapy & Allied Technologies, Review vol. 24, no. 1, pp. 45-53, Feb 2015.

[18] B. J. J. Abdullah et al., "Robot-assisted radiofrequency ablation of primary and secondary liver tumours: early experience," European Radiology, Article vol. 24, no. 1, pp. 79-85, Jan 2014.

[19] S. Song, J. Tokuda, K. Tuncali, A. Yamada, M. Torabi, and N. Hata, "Design evaluation of a double ring RCM mechanism for robotic needle guidance in MRI-guided liver interventions," in 2013 IEEE/RSJ International Conference on Intelligent Robots and Systems, 3-7 Nov. 2013 2013, pp. 4078-4083.

[20] N. Hata et al., "Body-mounted robotic instrument guide for age-guided cryotherapy of renal cancer," Medical Physics, Article vol. 43, no. 2, pp. 843-853, Feb 2016.

[21] N. Hata, R. Hashimoto, J. Tokuda, and Ieee, "Needle guiding robot for MR-guided microwave thermotherapy of liver tumor using motorized remote-center-of-motion constraint," in IEEE International Conference on Robotics and Automation (ICRA), Barcelona, SPAIN, Apr 18-22 2005.

[22] E. Franco, D. Brujic, M. Rea, W. M. Gedroyc, and M. Ristic, "Needle-Guiding Robot for Laser Ablation of Liver Tumors Under MRI Guidance," Ieee-Asme Transactions on Mechatronics, Article vol. 21, no. 2, pp. 931-944, Apr 2016.

[23] S. Tovar-Arriaga, R. Tita, J. C. Pedraza-Ortega, E. Gorrostieta, and W. A. Kalender, "Development of a robotic FD-CT-guided navigation system for needle placement - preliminary accuracy tests," International Journal of Medical Robotics and Computer Assisted Surgery, Article vol. 7, no. 2, pp. 225-236, Jun 2011.

[24] R. Monfaredi et al., "A prototype body-mounted MRI-compatible robot for needle guidance in shoulder arthrography," in 5th IEEE RAS/EMBS International Conference on Biomedical Robotics and Biomechatronics, 12-15 Aug. 2014 2014, pp. 40-45.

[25] R. Monfaredi et al., "Development of a shoulder-mounted robot for MRI-guided needle placement: phantom study," International Journal of Computer Assisted Radiology and Surgery, Article vol. 13, no. 11, pp. 1829-1841, Nov 2018.

[26] G. Li et al., "Body-mounted robotic assistant for MRI-guided low back pain injection," International Journal of Computer Assisted Radiology and Surgery, vol. 15, no. 2, pp. 321-331, 2020/02/01 2020.

[27] B. Duan et al., "Image-guided Robotic System for Radiofrequency Ablation of Large Liver Tumor with Single Incision," in 12th International Conference on Ubiquitous Robots and Ambient Intelligence (URAI), Goyang, SOUTH KOREA, Oct 28-30 2015.

[28] D. Stoianovici et al., "AcuBot: A Robot for Radiological Interventions," Robotics and Automation, IEEE Transactions on, vol. 19, pp. 927-930, 11/01 2003.

[29] M. D. O. Leary, C. Simone, T. Washio, K. Yoshinaka, and A. M. Okamura, "Robotic needle insertion: effects of friction and needle geometry," in 2003 IEEE International Conference on Robotics and Automation (Cat. No.03CH37422), 14-19 Sept. 2003.

[30] R. J. Iii, J. Memisevic, and A. Okamura, Design Considerations for Robotic Needle Steering. 2005, pp. 3588-3594.

[31] N. Abolhassani, R. Patel, and M. Moallem, "Trajectory generation for robotic needle insertion in soft tissue," in The 26th Annual International Conference of the IEEE Engineering in Medicine and Biology Society, 1-5 Sept. 2004 2004, vol. 1, pp. 2730-2733.

[32] D. Glozman and M. Shoham, "Image-Guided Robotic Flexible Needle Steering," IEEE Transactions on Robotics, vol. 23, no. 3, pp. 459-467, 2007.

[33] A. Majewicz, T. R. Wedlick, K. B. Reed, and A. M. Okamura, "Evaluation of Robotic Needle Steering in ex vivo Tissue," IEEE International Conference on Robotics and Automation, vol. 2010, pp. 2068-2073, 2010.

[34] R. Alterovitz, K. Goldberg, and A. Okamura, Planning for Steerable Bevel-tip Needle Insertion Through 2D Soft Tissue with Obstacles. 2005, pp. 1640-1645.

[35] C. Riviere, A. Thakral, I. Iordachita, G. Mitroi, and D. Stoianovici, "Predicting respiratory motion for active canceling during percutaneous needle insertion," in 2001 Conference Proceedings of the 23rd Annual International Conference of the IEEE Engineering in Medicine and Biology Society, 2001, vol. 4: IEEE, pp. 3477-3480.

[36] B. Cagneau, N. Zemiti, D. Bellot, and G. Morel, "Physiological motion compensation in robotized surgery using force feedback control," in Proceedings 2007 IEEE International Conference on Robotics and Automation, 2007: IEEE, pp. 1881-1886.

[37] Y. J. Kim, J. H. Seo, H. R. Kim, and K. G. Kim, "Impedance and admittance control for respiratory-motion compensation during robotic needle insertion–a preliminary test," The

International Journal of Medical Robotics and Computer Assisted Surgery, vol. 13, no. 4, p. e1795, 2017.

[38] S. F. Atashzar, I. Khalaji, M. Shahbazi, A. Talasaz, R. V. Patel, and M. D. Naish, "Robot-assisted lung motion compensation during needle insertion," in 2013 IEEE International Conference on Robotics and Automation, 2013: IEEE, pp. 1682-1687.

[39] R. Odenbach, Y. Chen, S. Sengupta, R. Webster, E. J. Barth, and M. Friebe, 3D-printed Z-frame marker for MRI-guided interventions. 2017.

[40] B. Maurin et al., "A Patient-Mounted Robotic Platform for CT-Scan Guided Procedures," IEEE Transactions on Biomedical Engineering, vol. 55, no. 10, pp. 2417-2425, 2008.

[41] Y. Chen, I. S. Godage, Z. T. H. Tse, R. J. Webster, and E. J. Barth, "Characterization and Control of a Pneumatic Motor for MR-Conditional Robotic Applications," IEEE/ASME Transactions on Mechatronics, vol. 22, no. 6, pp. 2780-2789, 2017.

[42] M. Ilan E. "Core[X,Y]." https://corexy.com/index.html

[43] Y. Chen et al., "MRI-Guided Robotically Assisted Focal Laser Ablation of the Prostate Using Canine Cadavers," IEEE Trans Biomed Eng, vol. 65, no. 7, pp. 1434-1442, Jul 2018.

[44] Y. Chen et al., "Robotic System for MRI-guided Focal Laser Ablation in the Prostate," IEEE/ASME transactions on mechatronics : a joint publication of the IEEE Industrial Electronics Society and the ASME Dynamic Systems and Control Division, vol. 22, no. 1, pp. 107-114, 2017.

[45] D. B. Comber, J. E. Slightam, V. R. Gervasi, J. S. Neimat, and E. J. Barth, "Design, Additive Manufacture, and Control of a Pneumatic MR-Compatible Needle Driver," IEEE Transactions on Robotics, vol. 32, no. 1, pp. 138-149, 2016.

[46] P. Giraud and A. Houle, "Respiratory Gating for Radiotherapy: Main Technical Aspects and Clinical Benefits," ISRN Pulmonology, vol. 2013, p. 519602, 2013/03/19 2013.

[47] S. S. Vedam, V. R. Kini, P. J. Keall, V. Ramakrishnan, H. Mostafavi, and R. Mohan, "Quantifying the predictability of diaphragm motion during respiration with a noninvasive external marker," Med Phys, vol. 30, no. 4, pp. 505-13, Apr 2003.

[48] J. F. Wilson, "Mechanics of bellows: A critical survey," International Journal of Mechanical Sciences, vol. 26, no. 11, pp. 593-605, 1984/01/01/ 1984.

[49] W. C. Young and R. Budynas, Roark's Formulas for Stress and Strain (7th Edition). New York, USA: McGraw-Hill Professional Publishing, 2001.

[50] L. H. Poniatowski, S. S. Somani, D. Veneziano, S. McAdams, and R. M. Sweet, "Characterizing and Simulating Needle Insertion Forces for Percutaneous Renal Access," J Endourol, vol. 30, no. 10, pp. 1049-1055, Oct 2016.

[51] A. M. Okamura, C. Simone, and M. D. O'Leary, "Force modeling for needle insertion into soft tissue," IEEE Trans Biomed Eng, vol. 51, no. 10, pp. 1707-16, Oct 2004.

[52] Y. Kobayashi, T. Sato, and M. G. Fujie, "Modeling of friction force based on relative velocity between liver tissue and needle for needle insertion simulation," Conf Proc IEEE Eng Med Biol Soc, vol. 2009, pp. 5274-8, 2009.

[53] Y. Chen, I. S. Godage, S. Sengupta, C. L. Liu, K. D. Weaver, and E. J. Barth, "MR-conditional steerable needle robot for intracerebral hemorrhage removal," International Journal of Computer Assisted Radiology and Surgery, vol. 14, no. 1, pp. 105-115, 2019/01/01 2019.

[54] B. Carstensen, "Repeatability, reproducibility and coefficient of variation," Comparing Clinical Measurement Methods: A Practical Guide, pp. 107–114, 2010.

[55] H. W. Kenneth, T. Jonathan, Z. Hui James, V. Emmanuel, and R. C. Kevin, "Prediction of 3D internal organ position from skin surface motion: results from electromagnetic tracking studies," in Proc.SPIE, 2005, vol. 5744.